Mechanical Systems and Signal Processing 187 (2023) 109921

Contents lists available at ScienceDirect

Mechanical Systems and Signal Processing

journal homepage: www.elsevier.com/locate/ymssp

Event-driven MEMS vibration sensor: Integration of triboelectric nanogenerator and low-frequency switch

Mohammad Mousavi [a], Mohammad Alzgool [a], Benyamin Davaji [b], Shahrzad Towfighian [a,*]

[a] Binghamton University, 4400 Vestal Parkway East, Binghamton, NY 13902, United States of America
[b] Northeastern University, 360 Huntington Ave, Boston, MA 02115, United States of America

ARTICLE INFO

Communicated by W. Ostachowicz

Keywords:
TENG
Shock sensing
Vibration sensing
MEMS low-frequency switch
Self-powered
Energy harvester

ABSTRACT

Triboelectric-nano-generator (TENG) is able to produce a very small current and a large voltage compared to piezoelectric or electromagnetic generators. The large voltages from the TENGs are suitable for operating MEMS devices without external AC or DC generators. Producing micro-sized TENG using MEMS fabrication process enables integration of them with MEMS sensors and actuators. This combination is useful because the required voltage for driving MEMS is obtained from the motion of the event that is being measured. In this work, an event-driven vibration sensor is introduced which actuates a switch as the frequency or amplitude of the vibration exceeds a desired threshold. Using CMOS micromachining, a 1.5 mm × 1.5 mm TENG in contact-separation (CS) mode is fabricated to convert ambient vibrations to a voltage generated between a conductive aluminum layer and a dielectric Polyimide layer. The large generated voltage between the electrodes can operate a low-frequency electrostatic MEMS switch. Two events are able to produce the resonant dynamic pull-in needed to close the switch. Event one is when the input amplitude exceeds the dynamic pull-in threshold which is called acceleration sensitive mode. Event two is when the frequency of the vibration exceeds a specified threshold. An electromechanical model for the MEMS switch part of the vibration sensor is also presented. Results show that MEMS-TENG is able to supply the MEMS switch in the frequency sensitive and acceleration sensitive modes with a good signal-to-noise-ratio, sensitivity, and accuracy.

1. Introduction

Random, low-frequency environmental mechanical energy is convertible into an electrical signal using the triboelectric nano-generator (TENG) invented by Wang [1]. Using the open-circuit mode of TENG, the generated voltage can be considered as a useful energy transduction in today's world. In support of this idea, some features and references are reviewed in the following.

TENG has the advantage of small cost, diverse choice of materials, compatibility with the patterns of ambient mechanical energy, and broad range of applications [2]. Triboelectrification uses contact electrification and then takes advantage of electrostatic induction. Four TENG modes exist: vertical contact-separation (CS), lateral sliding-, single-electrode, and freestanding [3]. The method of energy harvesting depends on the type of the wasted energy of different environments. CS is applicable for many ambient disturbances especially those that carry the oscillatory motion such as walking, industrial machines, transportation machines. This

* Corresponding author.
E-mail addresses: smousav1@binghamton.edu (M. Mousavi), malzgoo1@binghamton.edu (M. Alzgool), b.davaji@northeastern.edu (B. Davaji), stowfigh@binghamton.edu (S. Towfighian).

https://doi.org/10.1016/j.ymssp.2022.109921
Received 18 May 2022; Received in revised form 26 October 2022; Accepted 28 October 2022

work investigates the application of the CS mode in micro scale contact area and its application in MEMS switches for self-driven sensing.

The importance of self-powered systems has been grown significantly with the emergence of internet of things (IoT) and aerospace exploration machines for the purposes of communication, observation, measurement, and actuation [4,5]. In IoT area, triboelectrification is considered as eco-friendly, efficient harvester of sustainable mechanical motions in the environment, and capable of being combined with other harvesting technologies [6].

In aerospace technology, there is a demand for self-powered systems using TENG [7]. Some advantages include multi-functionalities, low cost, and signal reliability of triboelectric self-powered sensors. In electronics, a hybrid system of triboelectric and electromagnetic generators was reported [8] where the generators operate an electronic watch with energy from the wrist motion. Energy harvesting from ambient acoustic noise was reported by Yang et al. [9] where a thin film is vibrated by pressure from acoustic waves. To create self-powered sensors, triboelectric transducers should merge with Micro-electro-mechanical systems (MEMS) electrostatic (capacitive) switches.

MEMS switches are low-powered micromachined systems that operate from signals generated by TENGs that are actuated by frequency signals ranging from a few cycles per second up to cycles in the GHz-scale. The switches close depending on whether the vibrations cause metal-on-metal contact. The electrostatic MEMS switches respond to the resonance bandwidth [10]. Some MEMS switches use resonance dynamic pull-in phenomenon to close the switch and pass a current. The application of resonance dynamic pull-in in MEMS switches are in wireless communication [11], mass-sensors [12] and gas-sensors [13]. Mechanical vibrations can be measured as an electrical signal via a transducer [4,14]. The signal is amplified and delivered to the MEMS switch terminals.

The triboelectric generators in meso [15] and micro-scale (current work) operate MEMS switches. However, because of the sensitivity of the MEMS-TENG presented in the current work, the generated signal can be used as frequency signals applicable for resonant bandwidth of the MEMS switch. However in the meso scale version, because of the frequency response of the TENG with high amplitudes at low frequencies, the output is not suitable for radio frequency applications. It should be noted that in comparison with the proposed MEMS-TENG, using TENG in meso scale requires much larger environmental vibrations and much lower frequency and provides less sensitivity and is not suitable for integration with MEMS.

CMOS compatible micro-fabrication techniques can be used to scale down TEGs to micro-scale for integration with MEMS switches. However, the triboelectric mechanisms that have been used so far were not made in MEMS scale. The smallest device dimensions was reported $3\ \text{mm} \times 5\ \text{mm}$. The feasibility of the micro scale triboelectric systems in CS mode was presented by Hamid et al. [16] via simulations and experiments [17]. A triboelectric generator in micro scale (MEMS-TENGs) is a good candidate for a reliable power source of conventional MEMS devices. They are also advantageous because of integration compatibility with other electronic components on the same chip such as MEMS switches [18]. A self-powered MEMS optical modulation is developed using TENG in sliding-mode [19]. The results are promising except the TENG size which is in meso scales and therefore is not compatible with the size of the actuators. Yang et al. [20] created a 1-cm-motor rotating with fast frequency and supplied with a TENG in sliding-mode with low frequency. The results showed the successful application of $18.5\ \text{cm} \times 18.5\ \text{cm}$ TENG for supplying micro actuators using low frequency signals. However, driving a micro motor using a generator 30 times larger is not practical. The triboelectric generators in micro scale can reach high power density and noticeable voltage generation in high frequency bandwidths. The high voltage and low current are apt for driving electrostatically actuated MEMS [21]. The electrostatic actuation uses capacitive forces between charged electrodes, and require voltage input with no electrical current. This property makes them ideal to be merged with TENG as apposed to piezoelectric or electromagnetic transducers [15,17,22].

The novelty of the proposed work is the adoption of micromachining techniques to enable integration of MEMS-TENG with electrostatic MEMS sensors and actuators. In this work, we present how vibration sensors can be made autonomous for applications in real-time condition monitoring. A triboelectric generators provides the voltage needed by a capacitive actuator. Unlike previous works on MEMS switches [10–13] that provided the AC voltage from a function generator, our system is autonomous, i.e. the MEMS-TENG produces a voltage signal once subjected to mechanical motion. In addition, TENG in micro-scale is a more sensitive sensor (has a high signal to noise ratio) compared to the large-scale sensors in monitoring mechanical motions. We used CMOS-compatible technologies for fabricating the TENG, which allows mass production and compatibility with other electronic components. This is a great achievement towards miniaturization trend that opens doors to many innovative self-powered mechanical sensors.

This paper is organized as follows. The proposed vibration sensor is depicted and detailed in Section 2. Also, a mathematical model is presented for the MEMS switching part of the device. Section 3 explains the testing setup for the experiments. The results are reported in Section 4 and discussed in this section. At the end, the conclusion from results and perspectives are presented.

2. Mechanism and modeling

Environmental and machinery vibrations are prone to structural faults and disturbances that affect their response. We propose a vibration sensor that is autonomous and self-powered. The vibration sensor consists of two subsystems, MEMS-TENG and MEMS switch. Oscillatory motion from a base is transmitted to the MEMS-TENG and causes contact between the triboelectric layers as in Fig. 1(b). The contact-separation generates a voltage between the TENG electrodes which is an indicator of the vibration frequency or amplitude. The generated signal is biased ($+V_{DC}$) in a passive summer circuit Fig. 1(c). Because of the high amplitude and large signal-to-noise ratio found in the triboelectric voltage signal, it is capable of driving an electrostatic MEMS such as a MEMS switch Fig. 1(d). The electrostatic forces generated by the electric field created by something actuate the electrostatic MEMS switch. The MEMS switch receives the vibration amplitude and frequency information through the MEMS-TENG output signal. This system can

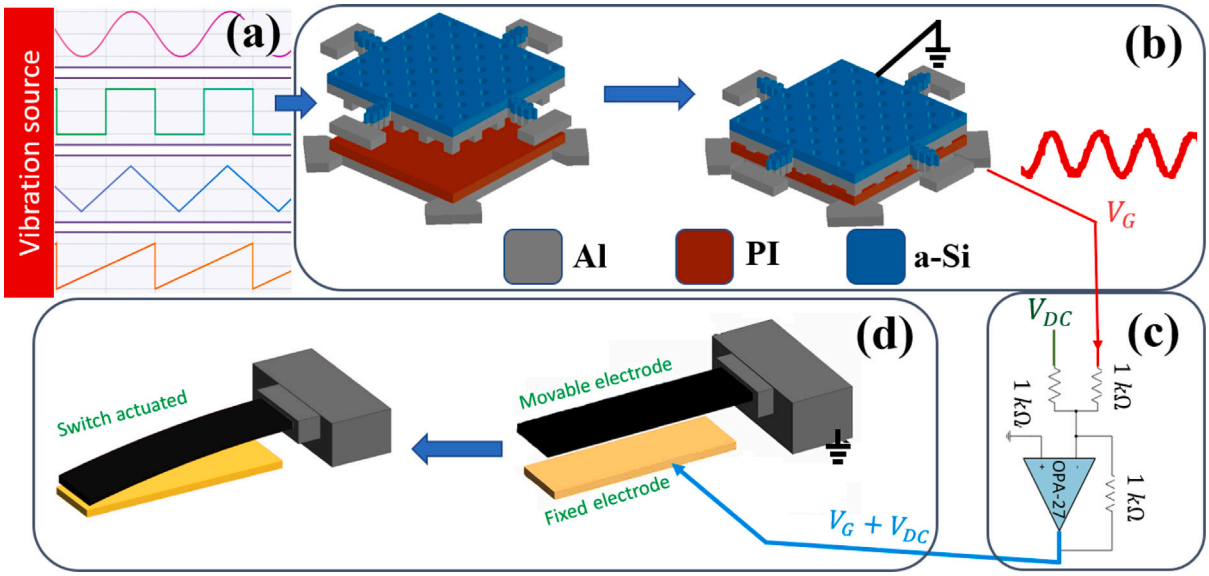

Fig. 1. Schematic of the MEMS vibration sensor. Part (a) shows different sources of vibration. Part (b) the MEMS-TENG before and after contact-separation. Part (c) shows a summer circuit which adds up a DC voltage V_{DC} to the generated voltage and sends the output to the MEMS switch. Part (d) shows the schematic of the MEMS switch used as the actuator part of the developed vibration sensor before and after switching.

Table 1
Dimensions of the MEMS-TENG.

Parameter	Symbol	Value
Side length	l	1500 μm
Triboelectric layer thickness	t_T	5 μm
Gap	D	2 μm
Top-electrode thickness	t_1	100 nm
Proof mass thickness	t_2	1 μm
Bottom-electrode thickness	t_3	200 nm
Fundamental frequency	f_G	0.8 kHz

be adjusted to become sensitive to the input amplitude or frequency in a way that the switch is closed as the amplitude or frequency exceeds a threshold.

The MEMS-TENG we used in this work (see Table 1) consists of a movable electrode and a fixed electrode. The contact and separation between the electrodes cause the accumulation of charges over each electrode and a potential difference is generated. The environmental vibration as an external excitation causes the contact-separation of the TENG electrodes.

The MEMS switch is an electrostatically actuated microcantilever which is mounted on an anchor. At the bottom and parallel to the microcantilever, a conductive fixed layer is fabricated for driving using electrostatic force. The switch fixed and movable electrodes are connected to the TENG terminals for the conversion of the environment mechanical vibrations to the switch actuation. The fabrication details of the MEMS switch and MEMS-TENG will be introduced in Section 3.

The operation principle is that the switch is closed when the applied voltage exceeds the pull-in instability threshold or when the instantaneous switch state including its position and velocity exceed instability thresholds [23].

Assume w is the displacement of the tip of the beam. Eq. (1) shows the equation of motion of a cantilevered beam as a continuous system to which a distribution electrostatic force $f_e(w,x,t)$ is applied. We present a model to describe the motion.

$$\rho_s A_s \frac{\partial^2 w}{\partial t^2} + c_s \frac{\partial w}{\partial t} + E_s I_s \frac{\partial^4 w}{\partial x^4} = f_e(w,x,t) \tag{1}$$

The parameters are listed in Table 2. The following boundary conditions should be satisfied for the MEMS switch: $w(0,t) = 0$, $\frac{\partial w(0,t)}{\partial x} = 0$, $\frac{\partial^2 w(L,t)}{\partial x^2} = 0$, $\frac{\partial^3 w(L,t)}{\partial x^3} = 0$. Considering the first transverse mode of the cantilever and using the Galerkin's reduced-order method, the relative motion, $y(t)$, between the base and the switch movable electrode is modeled by a second-order ordinary differential as:

$$m_s \ddot{y} + c_s \dot{y} + k_s y = F(V_{DC}, V_G, y) = -\frac{\epsilon A (V_{DC} + V_G)^2}{2(d+y)^2} \tag{2}$$

Table 2
MEMS switch properties.

Parameter	Symbol	Value
Beam length	L	505 μm
Beam width	b_1	20.5 μm
Beam thickness	h_1	2 μm
Module of elasticity	E	160 GPa
Density	ρ	2330 kg/m^3
Initial gap	d	2 μm
Bottom electrode width	b_2	32 μm
Electrode thickness	h_2	0.5 μm
Electrode area	A	1.025×10^{-8} m^2

The symbols d, m_s, c_s, k_s, A represent the initial gap and the equivalent mass, damping, stiffness, and electrode surface area. $\epsilon = 8.85 \times 10^{-12}$ F/m is the vacuum permittivity. The reduced-order electrostatic force is a function of the DC bias voltage, MEMS-TENG generated voltage, and the MEMS switch displacement. Setting the damping coefficient to zero and using the Jacobian matrix, the fundamental frequency of the system is calculated as a function of the nonlinear force as one can obtain:

$$f_s = \frac{1}{2\pi}\sqrt{\mathbf{Im}\left(\begin{vmatrix} 0 & 1 \\ -k_s + \frac{\epsilon A V_{DC}^2}{(d+y)^3} & 0 \end{vmatrix}\right)} \tag{3}$$

where **Im** denotes the imaginary part of the eigen-values of the Jacobian matrix that is the same as the fundamental switch frequency f_s. Using Eq. (3), the frequency shift is plotted in Fig. 5. By increasing the DC bias voltage, the MEMS switch fundamental frequency is reduced to zero at the pull-in voltage.

The analytical model in Eq. (1) is used for the MEMS switch characterization. Using the shooting method the frequency response of the MEMS switch is simulated. This method is chosen because the periodic actuation of a dynamic system is targeted. Shooting method searches for stable and unstable states of a system in the presence of specific linear and nonlinear conditions. It considers the initial condition as a tuning parameter needed to start solving the problem [24]. The system dynamics Eq. (1) is represented in state-space Eq. (4).

$$\begin{Bmatrix} X_1 \\ X_2 \end{Bmatrix} = \begin{Bmatrix} y \\ \dot{y} \end{Bmatrix} \tag{4}$$

As the shooting method initial condition vector, η_1 and eta_2 are defined as in Eq. (5).

$$\begin{Bmatrix} \eta_1 \\ \eta_2 \end{Bmatrix} = \begin{Bmatrix} X_1(0) \\ X_2(0) \end{Bmatrix} \tag{5}$$

The variation of the initial conditions in every solution should converge to zero. Therefore, $X_3 = \frac{\partial X_1}{\partial \eta_1}$, $X_4 = \frac{\partial X_1}{\partial \eta_2}$, $X_5 = \frac{\partial X_2}{\partial \eta_1}$, and $X_6 = \frac{\partial X_2}{\partial \eta_2}$ are defined. Then, the augmented system Eq. (6) including MEMS switch dynamics and variations are in an iterative procedure using Floquet Theory [24].

$$\begin{Bmatrix} \dot{X}_1 \\ \dot{X}_2 \\ \dot{X}_3 \\ \dot{X}_4 \\ \dot{X}_5 \\ \dot{X}_6 \end{Bmatrix} = \begin{Bmatrix} X_2 \\ -k_s X_1 - c_s X_2 - \frac{\beta(V_{DC}+V_G)^2}{(d+X_1)^2} \\ X_5 \\ X_6 \\ -k_s X_3 - c_s X_5 + 2X_3 \frac{\beta(V_{DC}+V_G)^2}{(d+X_1)^3} \\ -k_s X_4 - c_s X_6 + 2X_4 \frac{\beta(V_{DC}+V_G)^2}{(d+X_1)^3} \end{Bmatrix} \tag{6}$$

The error of the initial condition is updated in each frequency as in Eq. (7).

$$\begin{Bmatrix} \eta_1 \\ \eta_2 \end{Bmatrix}_{New} = \begin{Bmatrix} \Delta\eta_1 \\ \Delta\eta_2 \end{Bmatrix} + \begin{Bmatrix} \eta_1 \\ \eta_2 \end{Bmatrix}_{Old} \tag{7}$$

and the error is calculated as in Eq. (8).

$$\begin{Bmatrix} \Delta\eta_1 \\ \Delta\eta_2 \end{Bmatrix} = \begin{bmatrix} X_3 - 1 & X_4 \\ X_5 & X_6 - 1 \end{bmatrix}^{-1} \begin{Bmatrix} \eta_1 - X_1 \\ \eta_2 - X_2 \end{Bmatrix} \tag{8}$$

3. Micro-fabrication and experimental setup

In this work, we used a MEMS-TENG (see Table 1) fabricated in Cornell Nanofabrication Facility CNF (Fig. 2a). As shown in the schematic Fig. 2b, the TENG consists of a conductive layer, dielectric layer, and another conductive layer. The fabrication starts with an insulating layer of Aluminum Nitride (AlN) to eliminate leakage through the silicon wafer, the first conductive layer was made by

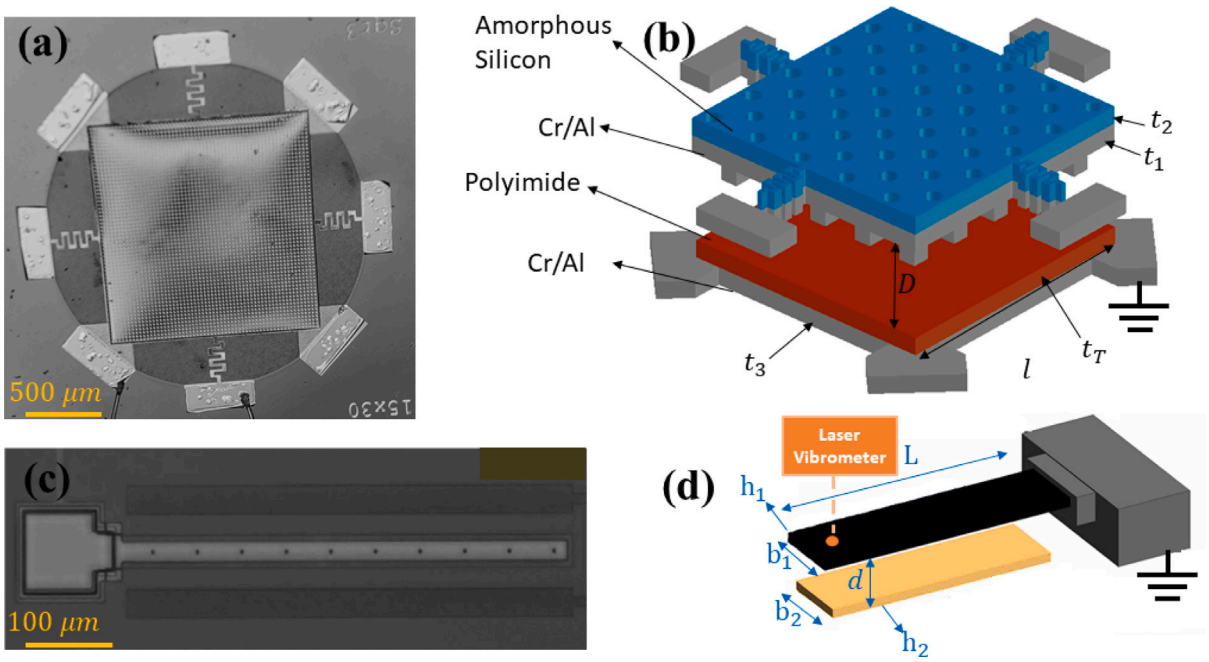

Fig. 2. Part (a) shows the optical image of the MEMS-TENG from the top view. Part (b) shows a schematic of the MEMS-TENG used to convert vibrational energy into electricity for the MEMS switch. Part (c) shows an image of the MEMS switch taken with the microscope of the laser vibrometer. There are two extra electrodes at the sides of the fixed electrode which are used for opening the MEMS switch by generating a strong electrostatic fringe-field effect [21] which are not effective in this work. Part (d) shows the schematic of the MEMS switch used as the actuator part of the vibration sensor. The dimensions are symbolized.

sputtering and patterning of 200 nm Chrome-Aluminum (Cr/Al), 5 μm dielectric layer of Polyimide (PI) was spun-coated and baked in polyimide oven, 2 μm sacrificial layer of Silicon oxide (SiO_2) was deposited with Plasma-Enhanced Physical-Vapor-Deposition (PECVD) to create the gap, this oxide layer was also patterned to create pins in the top electrode layer, the top conductive layer was formed by sputtering 120 nm Cr/Al, this Cr/Al was etched with serpentine springs to allow the layer to move vertically, 1 μm amorphous silicon (a-Si) on top electrode was deposited with PECVD as an elastic layer and a proof mass to absorb energy from vibrations, and finally, the device is released using vapor hydrofluoric acid (vHF) which will remove (SiO_2) and result in hanging structure. The static analysis and frequency response of the generator's top electrode indicate that the stiffness of the device springs is 38.37 N/m the fundamental frequency of the transverse motion is approximately 0.8 kHz. The MEMS switch Fig. 2c consists of a microcantilever, two fixed side electrodes and a fixed center electrode was fabricated by MEMSCAP using the PolyMUMPS process [25]. Optical imaging was used to measure the geometric dimensions and fabrication quality. The schematic and dimension symbols are shown in Fig. 2d. The properties and geometry of the MEMS switch can be found in Table 2. The experimental setup for testing the MEMS vibration sensor is illustrated in Fig. 3.

The MEMS-TENG is mounted and wired on a PCB. The PCB is installed on top of a mini-shaker (electro-dynamic mini-shaker 4810). The input signal to the shaker is manipulated in MATLAB and transferred to the shaker via a NI DAQ USB-6366 and a voltage amplifier. The MEMS-TENG generated voltage is added up to a DC voltage V_{DC} through an active summer circuit Fig. 1(c) where a OPA27 operational-amplifier and three 10 kΩ resistors are used. The MEMS switch is situated inside a vacuum chamber at $P = 150$ mTorr and the summer output voltage is applied to the MEMS switch. The MEMS-TENG operates in the ambient pressure. A laser doppler vibrometer measures the velocity of the switch tip, and send the output information to the DAQ.

4. Results and discussion

The performance of the MEMS-TENG is experimentally characterized in this work. The generated voltage V_G in the open-circuit state was measured in the presence of oscillatory base-excitation. The results at different frequencies and different base-acceleration amplitudes a_{base} are reported in Fig. 4. Intuitively, V_G is increased as the base-acceleration grows. Results also show a monotonic increase of V_G by increasing the base-excitation frequency. In this 3D graph, the peak to peak voltage reaches nearly 1.2 V at $a_{base} = 2.3$g and $f = 15$ kHz. The variation of V_G is smaller at greater base accelerations and slower frequencies. V_G can approximately be considered constant for $f > 5$ kHz and $a_{base} > 2.15$ g.

The MEMS-TENG performance is considerable compared with its meso-scale version made in a previous work at a much larger size [15]. The meso scale TENG (3.6 cm × 5 cm) was fabricated to absorb environment shocks and generate a voltage signal to actuate a MEMS switch. The size of the generator is 800 larger than the MEMS-TENG reported here. The results of the meso scale

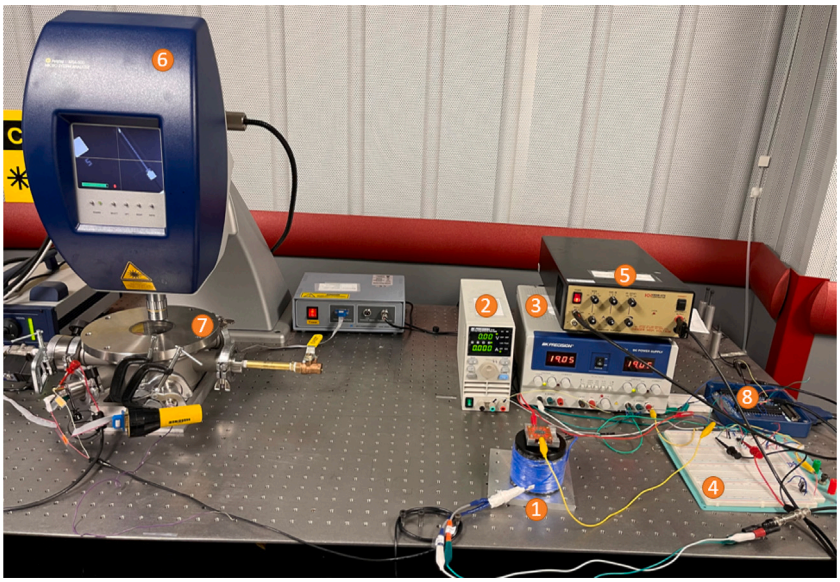

Fig. 3. Testing setup including: (1) Micro triboelectric generator mounted on electrodynamic mini-shaker. (2) DC power supply for generating V_{DC}. (3) Dual DC generator for supplying the summer circuit. (4) Inverting summer circuit. (5) Voltage amplifier for supplying the shaker. (6) Laser vibrometer. (7) Capacitive MEMS switch in the chamber. (8) Data acquisition system.

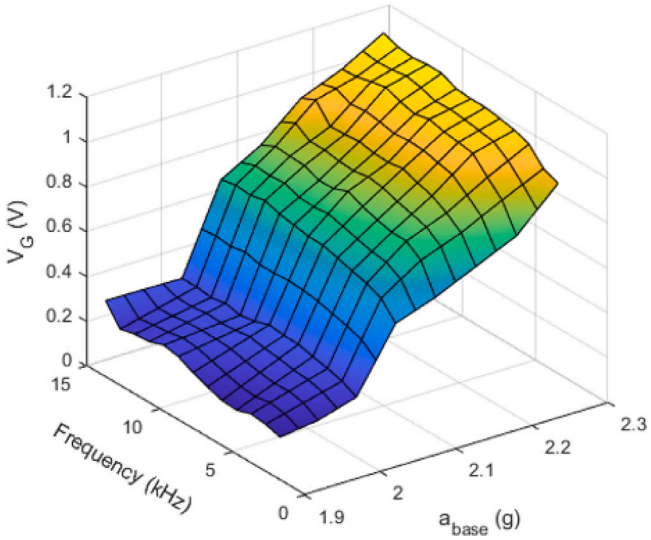

Fig. 4. Characterization of the MEMS-TENG in the presence of harmonic base-excitation (measured). The x-axis is the base-acceleration and the y-axis is the excitation frequency. The peak-to-peak generated voltage is shown by the z-axis.

TENG show that for less than a 4 g shock acceleration, the TENG does not generate any voltage because of the stiffness of the TENG structure. Comparing the sensitivity of the implemented TENG, our work gives 3 V/g as plotted in Fig. 4 while in the previous work, the sensitivity of the TENG is 4.4 V/g. The range of operation of meso-scale version is 4 g to 20 g. While the range of operation of the proposed MEMS-TENG is 2 g to 2.3 g. Because of the sensitivity of the MEMS-TENG presented in the current work, the generated signal can be used as frequency signals applicable for resonant bandwidth of the MEMS switch. It should be noted that in comparison with the proposed MEMS-TENG, using TENG in meso scale requires much larger environmental vibrations and lower vibration frequency.

For characterization of the vibration sensor as a result of integration of the MEMS-TENG and MEMS switch, two operation modes are evaluated. One mode is frequency sensitive and can be used to sense abnormal variations in the frequency of a machine's vibrations that should be almost constant. When the frequency exceeds the threshold, the switch closes.

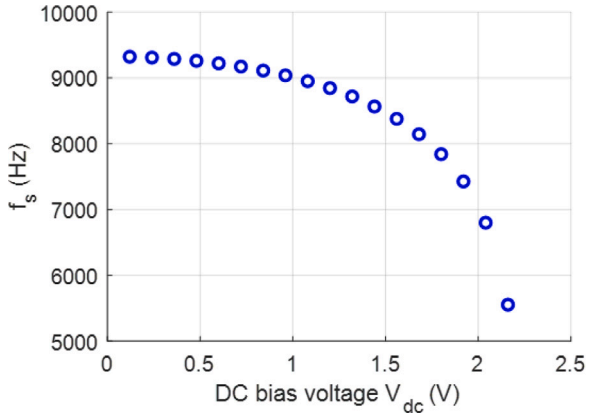

Fig. 5. The effect of DC bias voltage on the fundamental frequency applied on the MEMS switch.

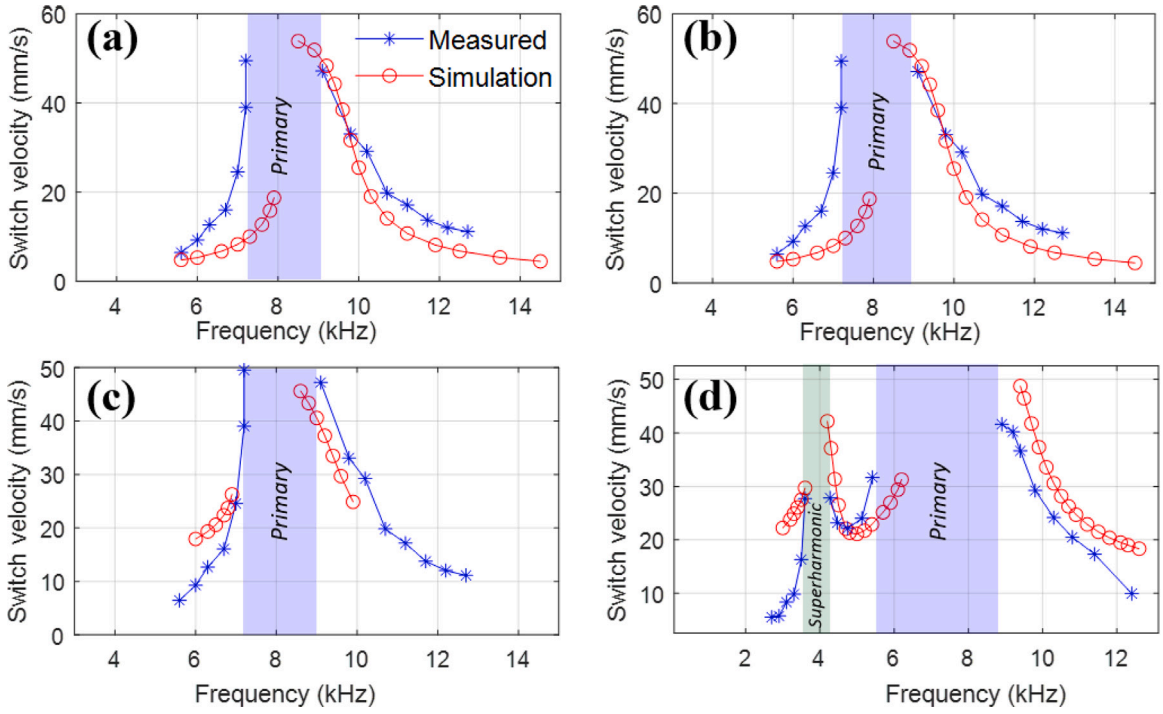

Fig. 6. Measurement and simulation of the vibration sensor frequency response. In the measurements (blue lines), the MEMS switch is actuated by the MEMS-TENG that is prone to 2.05 g and generates 0.6 V peak-to-peak. The simulation results (red graphs) show the frequency response and the resonance dynamic pull-in (also called inevitable escape region) in the presence of 0.3 V AC voltage that is half of the peak-to-peak value. Parts (a), (b), (c) are related to the primary resonance of the MEMS switch with V_{DC} = 1.6 V, V_{DC} = 1.7 V, and V_{DC} = 1.8 V, respectively. Part (d) shows a wider frequency range including primary and super-harmonic resonances with 0.4 V AC voltage and V_{DC} = 1.8 V. Part (d) illustrates a wider frequency range which includes the superharmonic resonance that happens at half of the primary resonance around 4 kHz. The simulation results successfully predict this nonlinear behavior. (For interpretation of the references to color in this figure legend, the reader is referred to the web version of this article.)

The second mode is acceleration sensitive. In this mode, the switch closes when the amplitude of the vibration passes a threshold. This mode is useful to assess the violence of a shock. It should be noted that the MEMS-TENG is mounted precisely perpendicular to the base plane and therefore, the characterization is conducted for a single axis (vertical) only. First, for the characterization of the MEMS switch, the nonlinear behavior of the capacitive actuation is required. As in Fig. 5, it shows the frequency shift of the MEMS switch in the presence of DC input.

Regarding the frequency sensitive mode, the dynamic model presented in Section 2 is validated as follows. As in [23,26–29], the frequency response of the MEMS switch is a part of the device characterization. Dynamic pull-in phenomenon is used for frequency detection for the primary, superharmonic and subharmonic resonances. The frequency response of the MEMS switch is analyzed in Fig. 6. The experimental data and simulation results are plotted with blue stars and red circles, respectively. The model tracks the

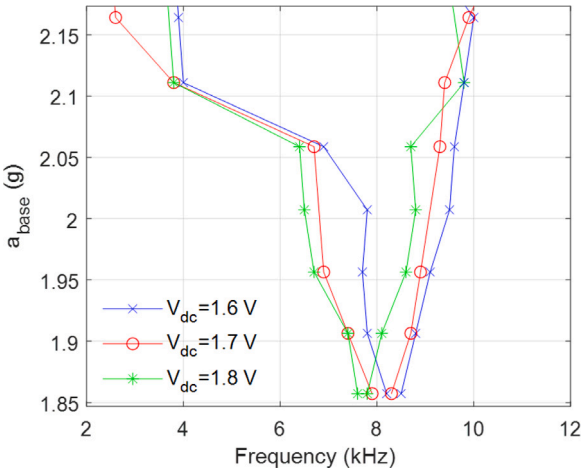

Fig. 7. Instability tongue of the vibration sensor operating at frequency sensitive mode (measured). The y-axis indicates the base-acceleration and the x-axis shows the resonance dynamic pull-in region where the MEMS switch is actuated and gets closed.

measured data with some deviations especially in the vicinity of the upper bound of the resonance dynamic pull-in region. Parts (a), (b), and (c) compare the effect of the initial DC voltage on the MEMS switch which is $V_{DC} = 1.6$ V, $V_{DC} = 1.7$ V, and $V_{DC} = 1.8$ V, respectively, on the frequency response and the resonance dynamic pull-in region. The measured results of these three parts are in the presence of a constant base-acceleration of $a_{base} = 2.05$ g under the MEMS-TENG. For simulation of the MEMS switch behavior, a sinusoidal signal with an amplitude of 0.3 V is fed as the AC input superimposed on the DC voltage Fig. 4. This figure shows that by increasing V_{DC}, the bandwidth of the switching region (inevitable escape) is increased because dynamic pull-in happens earlier as the switch electrodes get closer as a result of V_{DC}. The operation of the frequency-sensitive mode is demonstrated in videos presented at supplementary materials. In the attached video, Experiment 1 shows voltage generation of the MEMS-TENG and the MEMS switch response on an oscilloscope in two different channels. The operation of the vibration sensor when the excitation frequency exceeds lower and upper limits are shown in Experiment 2 and Experiment 3, respectively.

The reason for presenting MEMS switch velocity instead of displacement is the Laser Doppler drifting which appears when displacement measurement is used. This problem does not exist for the velocity measurement. Obviously, the model predicts a shorter bandwidth for the primary resonance dynamic pull-in compared to the measurements from the vibration sensor. One possibility is structural inaccuracies in the MEMS switch fabrication process such as thermal stress and curvature, which have not been taken into account in the model. The transient response of the MEMS switch after activating the base-excitation is another possibility, while the shooting method only considers the steady-state response. The third possibility can be the electrostatic force model which only considers the parallel-plate capacitive force [23]. While a more realistic model involves the electrostatic fringe-field effect. Fourth possibility is about the MEMS-TENG output. The AC output of the MEMS-TENG looks like periodic impulses rather than pure sinusoidal shape, and consequently, it affects the transient behavior of the MEMS switch. Such phenomenon influences the resonance dynamic pull-in instability and the filtering bandwidth of the switch.

For characterization of the vibration sensor in environments with different base-acceleration amplitudes, instability tongue is plotted which indicates the resonance dynamic pull-in (x-axis) versus the base-acceleration (y-axis). Measured results for $V_{DC} = 1.6$V, $V_{DC} = 1.7$ V, and $V_{DC} = 1.8$ V are graphed in Fig. 7. The vibration sensor is a band-pass filter that passes a bandwidth by closing the MEMS switch and remains OFF outside the bandwidth. By increasing the base-acceleration, the upper limit is increased and the lower limit is decreased. The superharmonic resonance becomes effective as the base-acceleration reaches $a_{base} = 2.1$ g and results in extension of the resonance-dynamic pull-in. The bandwidth boundaries is tunable by V_{DC}, e.g. at $a_{base} = 2.07$ g, the intervals of $\{7.8\ \text{kHz}, 9.5\ \text{kHz}\}$ centered at $f = 8.4$ kHz, $\{6.7\ \text{kHz}, 9.1\ \text{kHz}\}$ centered at $f = 8.1$ kHz, and $\{6.5\ \text{kHz}, 8.8\ \text{kHz}\}$ centered at $f = 7.8$ kHz, are obtained with $V_{DC} = 1.6$ V, $V_{DC} = 1.7$ V, and $V_{DC} = 1.8$ V, respectively.

The frequency sensitive mode of the proposed device needs a signal from something to actuate the RF MEMS switch. For this purpose, the ideal generator is expected to give a constant amplitude at the operation bandwidth of the device. Fig. 8 shows that at constant external vibration amplitudes, the output of the MEMS-TENG is a uniform amplitude signal that can be approximated with a constant value. The dashed lines indicate the uniform generated voltage in the frequency bandwidth (more than 5 kHz). For the vibrations with the amplitudes of 2.06 g, 2.14 g, and 2.21 g result in a uniform MEMS-TENG performance of 0.65 V, 0.85 V, and 1.05 V, respectively. The results show that the operation range of the proposed device in the frequency sensitive mode is between $a_{base} \in (2\ \text{g}, 2.3\ \text{g})$ and $f \in (5\ \text{kHz}, 15\ \text{kHz})$.

The vibration sensor in the frequency sensitive mode is presented in time-domain in Fig. 9 where the MEMS-TENG vibrates by $a_{base} = 2.21$ g base-acceleration and different frequencies. The blue line are the MEMS-TENG output and the red graphs are MEMS switch time–history. Part (a) shows the vibration sensor operation with $V_{DC} = 1.7$ V where resonance dynamic pull-in happens at $f = 10.6$ kHz. More details describing the switching operation is shown in part (b). The switching time for this experiment is 140 μs.

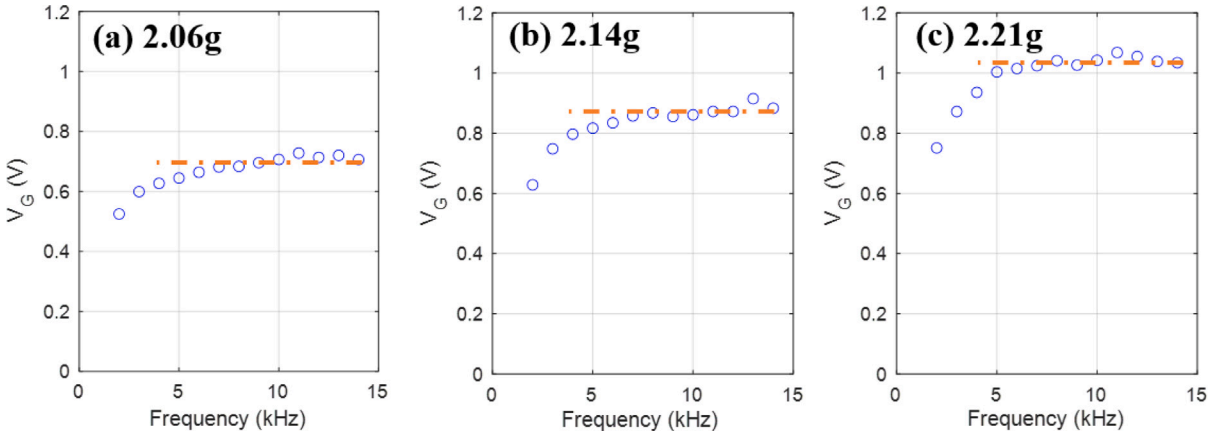

Fig. 8. Measured MEMS-TENG performance in the presence of constant amplitude external vibrations at different frequencies. The dashed red lines indicate an approximate value of the generated voltage. Part (a) shows a_{base} = 2.14 g. Part (b) shows a_{base} = 2.06 g. Part (c) shows a_{base} = 2.21 g. (For interpretation of the references to color in this figure legend, the reader is referred to the web version of this article.)

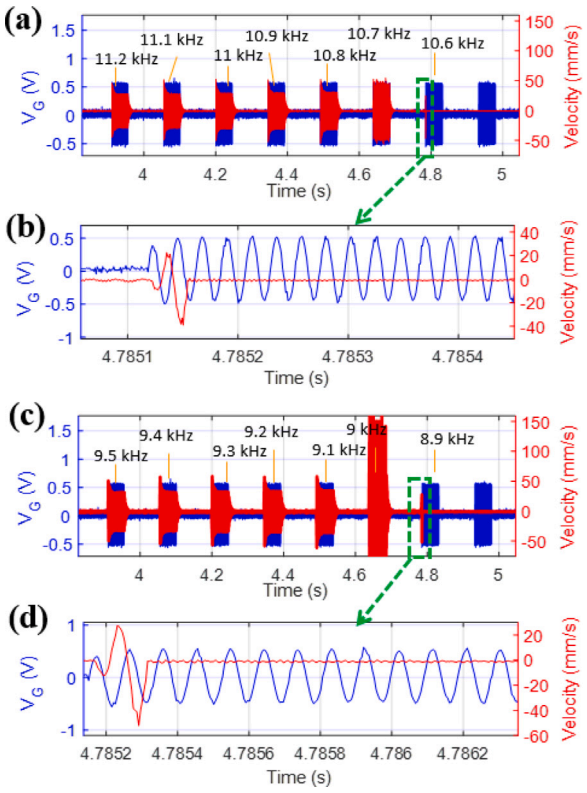

Fig. 9. MEMS switch and MEMS-TENG measured time response in the presence of a_{base} = 2.21 g base-excitation. Part (a) indicates the MEMS-TENG performance on the left axis and the MEMS switch response on the right axis with V_{DC} = 1.6 V. Part (b) shows a magnified view of the switching operation of part (a). Part (c) indicates the MEMS-TENG performance on the left axis and the MEMS switch response on the right axis with V_{DC} = 1.7 V. Part (d) shows a magnified view of the switching operation of part (c). (For interpretation of the references to color in this figure legend, the reader is referred to the web version of this article.)

Part (c) is the operation with V_{DC} = 1.6 V where the switch operates at f = 8.9 kHz. The magnified view of the switching process is illustrated in part (d). The switching time for this experiment is 150 μs.

The second application of the proposed vibration sensor is a self-driven acceleration sensitive MEMS filter. Depending on the frequency response of the MEMS-TENG and MEMS switch, as well as the DC bias voltage applied on the MEMS switch, the MEMS switch resonance dynamic pull-in occurs at different threshold shock accelerations. The required base-acceleration amplitude for closing the MEMS switch actuated at different frequencies is plotted in Fig. 10. The blue line shows the required base-acceleration

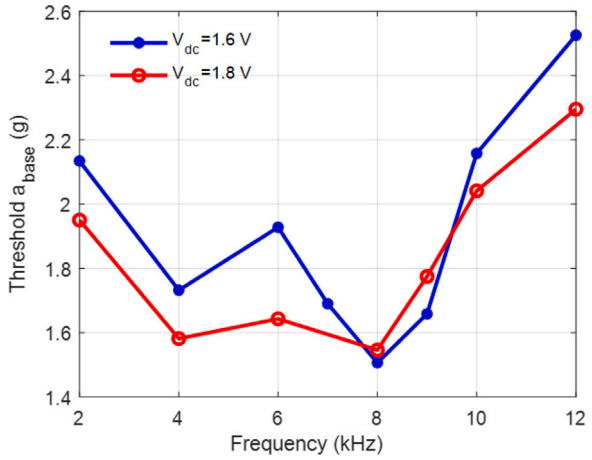

Fig. 10. Vibration sensor at the acceleration sensitive mode (measured). Base-acceleration threshold (y-axis) required for actuating the MEMS switch and resonance dynamic pull-in, at different excitation frequencies (x-axis). (For interpretation of the references to color in this figure legend, the reader is referred to the web version of this article.)

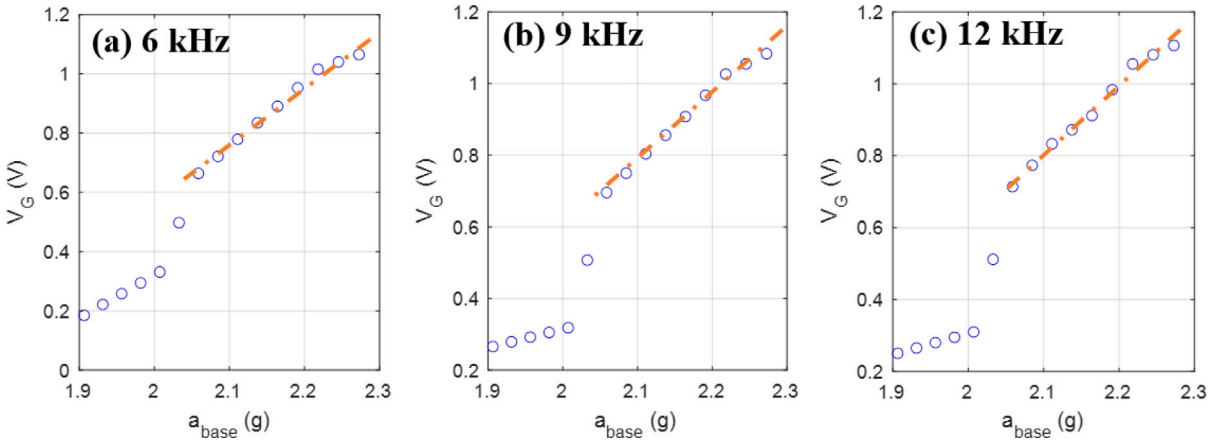

Fig. 11. Measured MEMS-TENG performance in the presence of constant frequency external vibrations at different accelerations. The dashed red lines indicate a line fit on the measured data. The excitation frequency is (a) 6 kHz; (b) 9 kHz; (c) 12 kHz.

for resonance dynamic pull-in at different frequencies in the presence of $V_{DC} = 1.6$ V. This result includes two minima at the vicinity of 8 kHz and 4 kHz. The first one is due to the primary resonance of the MEMS switch (see Fig. 5d) and the latter shows the superharmonic phenomenon which happens when the excitation frequency is half of the primary resonance. A similar trend is observed at $V_{DC} = 1.8$ V with less threshold base-acceleration, because the MEMS switch parallel-plates are already closer to each other compared to $V_{DC} = 1.6$ V.

Considering the acceleration sensitive mode, an ideal generator produces an output voltage that varies linearly with the acceleration. Fig. 11 depicts the regions at constant frequencies, where the MEMS-TENG voltage varies linearly with the base acceleration. The exist two linear regions with different slopes at slow and fast accelerations. The dashed lines indicate the linear approximation of the MEMS-TENG generated voltage versus the base-acceleration. The results show that the operation range of the proposed device in the frequency sensitive mode is between $a_{base} \in (2\text{ g}, 2.3\text{ g})$. Regarding the operation frequency, according to Fig. 10, the linear variation is observed for when $f > 8$ kHz, as the threshold a_{base} monotonically increases with the frequency.

The time–history of the vibration sensor is illustrated in Fig. 12. Part (a) shows the condition of $V_{DC} = 1.6$ V and $f = 10$ kHz. During the increase in the base acceleration, the generated voltage is also increased and dynamic pull-in occurs at $a_{base} = 1.7$ g. Part (a) shows the condition of $V_{DC} = 1.8$ V and $f = 9$ kHz. In this case, the dynamic pull-in occurs at $a_{base} = 2.15$ g. Parts (c) and (d) demonstrate the discrete sweeping of the base acceleration. The vibration sensor behavior is consistent with Fig. 10 where the acceleration sensitive mode is experimentally characterized.

For acceleration sensitive mode, the noise of the measured voltage from the MEMS-TENG can be quantified by filtering out the signal around the input frequency. The error signal including noise is quantified by finding the root-mean-square-error (RMSE). The RMSE for the noise signal is found to be around 50 mV.

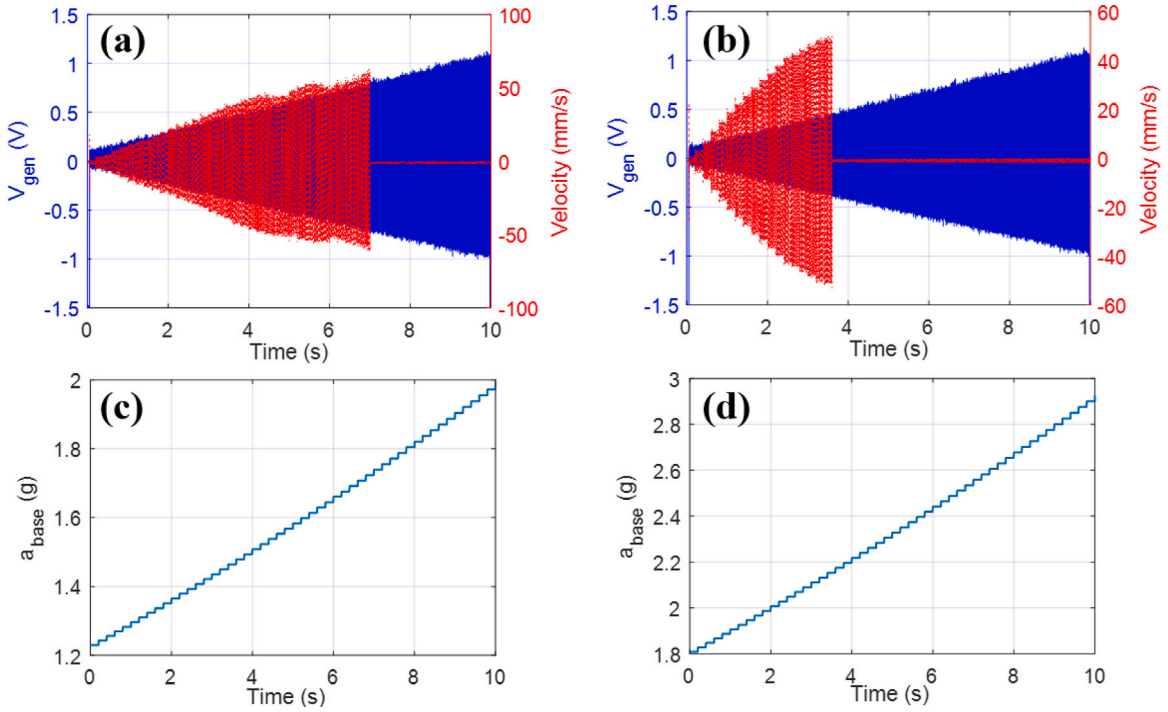

Fig. 12. Time-response of the vibration sensor in acceleration sensitive mode. Part (a) shows the time–history of the generate voltage and the MEMS switch during the incremental changes in the base acceleration with $V_{DC} = 1.6$ V and $f = 10$ kHz. Part (b) shows the time–history of the generate voltage and the MEMS switch during the incremental changes in the base acceleration with $V_{DC} = 1.8$ V and $f = 9$ kHz. Part (c) and Part (d) show the base acceleration of the MEMS-TENG corresponding to parts (a) and (b), respectively.

As shown in Fig. 13a, the vibration acceleration linearly changes over time. The MEMS-TENG output is measured at constant frequencies of $f = 2$ kHz (Fig. 13b) and $f = 9$ kHz (Fig. 13c). Using signal decomposition the noise signal was extracted and plotted (red). The RMSE algorithm in different frequencies in the bandwidth is plotted during the acceleration sweeping. The low value of RMSE for the noise, and because of the measured MEMS-TENG output voltage is around 1 V_{p-p}, we can conclude that the voltage measurements have a high signal-to-noise ratio of around 20. To overcome the high impedance issue of the triboelectric generator that causes very low currents, we rely on high-signal-to-noise-ratio voltage signal to enable effective integration of triboelectric generators and electrostatic actuators.

The proposed MEMS-TENG operates at small vibrations less than 3 g. For a practical demonstration of the MEMS-TENG response to base vibrations, we tested the MEMS-TENG on a cell-phone. Experiment 4 in the supplementary materials shows the performance of the MEMS-TENG mounted on an iPhone 12 PROMAX. As shown in Fig. 14, the generated voltage is indicated on the oscilloscope when the phone is ringing. The frequency and amplitude of the cell-phone is not constant when the phone rings and therefore different voltage signal shapes and amplitudes are generated. The generated voltage is in the order of 200–800 mV.

5. Conclusion and perspective

Event-driven MEMS vibration sensor is proposed in this work. The significant novelty of the proposed work is adoption of micromachining techniques to make a MEMS-TENG to miniaturize sensing and actuation which allowed easy integration with conventional electrostatic MEMS devices. In this work, we present how vibration sensors can be made autonomous for applications in real-time condition monitoring of machinery. A MEMS-TENG was integrated as a part of a complex system which replaces the power supply and motion sensing parts. The results show that the production of self-driven sensors and actuators using a single method of fabrication is feasible. MEMS devices are popular because of speed, sensitivity, fast frequencies, and small sizes. Utilizing micro-sized generators to supply electrostatic MEMS devices, with similar fabrication techniques enables billions of innovative devices be self-driven from various events. Miniaturizing mechanical systems enables high motion sensitivities. Because a MEMS-TENG can convert even small mechanical motions to electrical signals, the device reveals a great deal of information about fine vibrations. To experimentally evaluate the MEMS-TENG performance in the presence of base vibrations, it was mounted on a mini-shaker and a cell-phone and tested. As a prospective, the proposed vibration sensor can be applicable for fault detection of different machinery. Because of the tunability of the MEMS switch by means of the DC bias voltage where the threshold frequency or threshold amplitude is adjustable, the switching bandwidth is adjustable to desired intervals. Future works can include the squeeze-film damping effect, though it is not prominent for near-the-vacuum conditions. The vibration sensor can be characterized for the operation at different pressures. That characterization will allow a better understanding of integrated devices such as the presented vibration sensor.

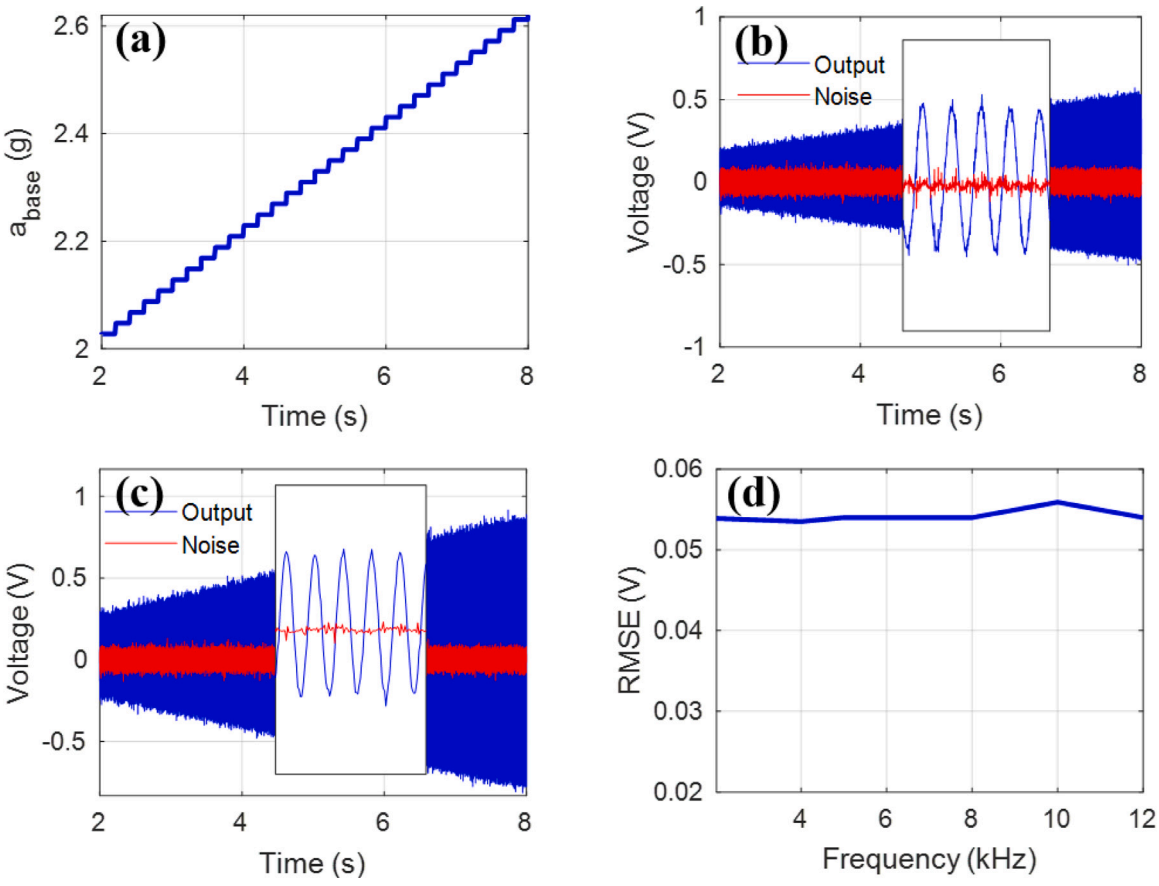

Fig. 13. (a) Acceleration of the external vibration, (b) MEMS-TENG output (blue) and noise (red) at 2 kHz, (c) MEMS-TENG output (blue) and noise (red) at 9 kHz, (d) noise RMSE for frequency range 2–12 kHz. (For interpretation of the references to color in this figure legend, the reader is referred to the web version of this article.)

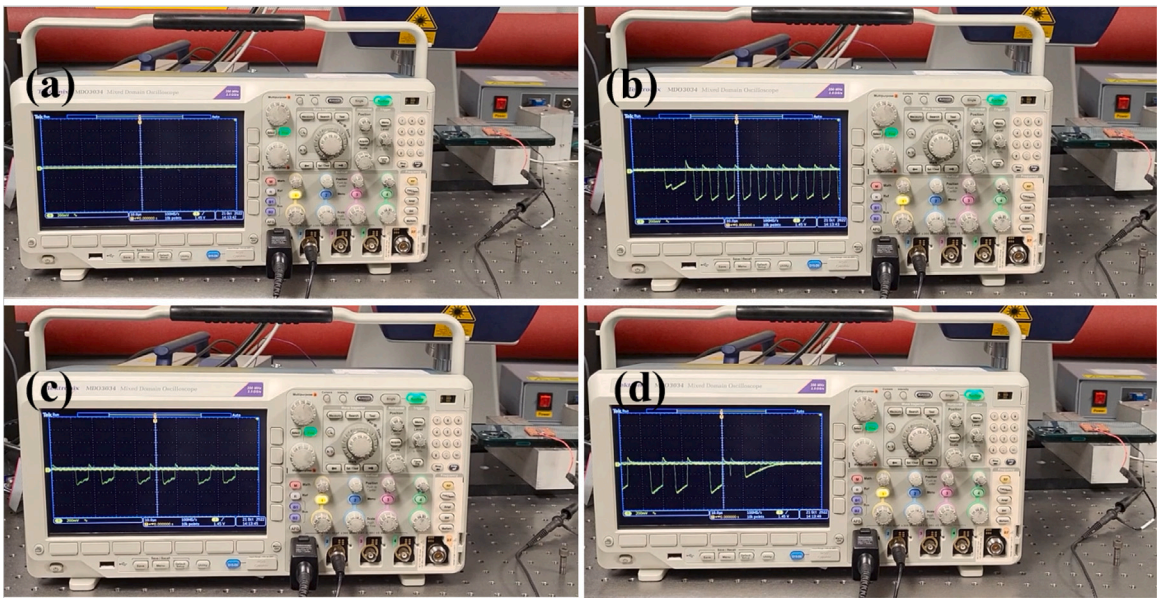

Fig. 14. Part (a) shows the initial state of the oscilloscope connected to the MEMS-TENG. Parts (b), (c), (d) show the MEMS-TENG voltage generation after the cellphone starts ringing and vibrating.

Declaration of competing interest

The authors declare that they have no known competing financial interests or personal relationships that could have appeared to influence the work reported in this paper.

Data availability

Data will be made available on request.

Acknowledgments

The authors would like to acknowledge the financial support of this study by National Science Foundation (NSF), USA through Grant 1919608. This work was performed in part at the Cornell NanoScale Science & Technology Facility, a member of the National Nanotechnology Coordinated Infrastructure, which is supported by the National Science Foundation, USA (Grant NNCI-2025233).

Appendix A. Supplementary data

Supplementary material related to this article can be found online at https://doi.org/10.1016/j.ymssp.2022.109921.

Here, the experimental results presented in the supplementary video are described. The video contains the results of testing the performance of the MEMS integrated vibrations sensor, in addition to testing the MEMS-TENG excited by cell-phone vibrations.The videos contain the experimental setup components including the MEMS-TENG mounted on the electrodynamic shaker, the MEMS switch, laser vibrometer. The generated voltage is measured with both oscilloscope and NI 6366 data acquisition system. In addition, the velocity of the MEMS switch tip is measured by the second channel of the oscilloscope as well as the data acquisition system.

References

[1] F.-R. Fan, Z.-Q. Tian, Z.L. Wang, Flexible triboelectric generator, Nano Energy 1 (2) (2012) 328–334.
[2] Z.L. Wang, L. Lin, J. Chen, S. Niu, Y. Zi, Triboelectric nanogenerator: single-electrode mode, in: Triboelectric Nanogenerators, Springer, 2016, pp. 91–107.
[3] C. Wu, A.C. Wang, W. Ding, H. Guo, Z.L. Wang, Triboelectric nanogenerator: a foundation of the energy for the new era, Adv. Energy Mater. 9 (1) (2019) 1802906.
[4] O. Rubes, J. Chalupa, F. Ksica, Z. Hadas, Development and experimental validation of self-powered wireless vibration sensor node using vibration energy harvester, Mech. Syst. Signal Process. 160 (2021) 107890.
[5] Y. Lo, Y. Shu, Self-powered SECE piezoelectric energy harvesting induced by shock excitation for sensor supply, Mech. Syst. Signal Process. 177 (2022) 109123.
[6] A. Ahmed, I. Hassan, M.F. El-Kady, A. Radhi, C.K. Jeong, P.R. Selvaganapathy, J. Zu, S. Ren, Q. Wang, R.B. Kaner, Integrated triboelectric nanogenerators in the era of the internet of things, Adv. Sci. 6 (24) (2019) 1802230.
[7] X. Hou, M. Zhu, L. Sun, T. Ding, Z. Huang, Y. Shi, Y. Su, L. Li, T. Chen, C. Lee, Scalable self-attaching/assembling robotic cluster (s2a2rc) system enabled by triboelectric sensors for in-orbit spacecraft application, Nano Energy 93 (2022) 106894.
[8] T. Quan, X. Wang, Z.L. Wang, Y. Yang, Hybridized electromagnetic–triboelectric nanogenerator for a self-powered electronic watch, Acs Nano 9 (12) (2015) 12301–12310.
[9] J. Yang, J. Chen, Y. Liu, W. Yang, Y. Su, Z.L. Wang, Triboelectrification-based organic film nanogenerator for acoustic energy harvesting and self-powered active acoustic sensing, ACS Nano 8 (3) (2014) 2649–2657.
[10] Z. Zhao, D.F. Wang, X. Lou, T. Ono, T. Itoh, An adjustable pre-stress based sensitivity enhancement scheme for cantilever-based resonant sensors, Mech. Syst. Signal Process. 146 (2021) 107002.
[11] L.-F. Wang, L. Han, J.-Y. Tang, Q.-A. Huang, Lateral contact three-state RF MEMS switch for ground wireless communication by actuating rhombic structures, J. Microelectromech. Syst. 22 (1) (2012) 10–12.
[12] M. Lyu, J. Zhao, N. Kacem, P. Liu, B. Tang, Z. Xiong, H. Wang, Y. Huang, Exploiting nonlinearity to enhance the sensitivity of mode-localized mass sensor based on electrostatically coupled MEMS resonators, Int. J. Non-Linear Mech. 121 (2020) 103455.
[13] N. Jaber, S. Ilyas, O. Shekhah, M. Eddaoudi, M.I. Younis, Resonant gas sensor and switch operating in air with metal-organic frameworks coating, J. Microelectromech. Syst. 27 (2) (2018) 156–163.
[14] Y. Fu, H. Ouyang, R.B. Davis, Triboelectric energy harvesting from the vibro-impact of three cantilevered beams, Mech. Syst. Signal Process. 121 (2019) 509–531.
[15] M. Mousavi, M. Alzgool, S. Towfighian, Autonomous shock sensing using bi-stable triboelectric generators and MEMS electrostatic levitation actuators, Smart Mater. Struct. 30 (6) (2021) 065019.
[16] H.A. Hamid, Z. Celik-Butler, Design and optimization of a MEMS triboelectric energy harvester for nano-sensor applications, in: 2019 IEEE Sensors Applications Symposium, SAS, IEEE, 2019, pp. 1–6.
[17] H.A. Hamid, Z. Çelik-Butler, A novel MEMS triboelectric energy harvester and sensor with a high vibrational operating frequency and wide bandwidth fabricated using UV-LIGA technique, Sensors Actuators A 313 (2020) 112175.
[18] T. Bu, H. Yang, W. Liu, Y. Pang, C. Zhang, Z.L. Wang, Triboelectric effect-driven liquid metal actuators, Soft Robot. 6 (5) (2019) 664–670.
[19] C. Zhang, W. Tang, Y. Pang, C. Han, Z.L. Wang, Active micro-actuators for optical modulation based on a planar sliding triboelectric nanogenerator, Adv. Mater. 27 (4) (2015) 719–726.
[20] H. Yang, Y. Pang, T. Bu, W. Liu, J. Luo, D. Jiang, C. Zhang, Z.L. Wang, Triboelectric micromotors actuated by ultralow frequency mechanical stimuli, Nature Commun. 10 (1) (2019) 1–7.
[21] M. Mousavi, M. Alzgool, S. Towfighian, Electrostatic levitation: an elegant method to control MEMS switching operation, Nonlinear Dynam. 104 (4) (2021) 3139–3155.
[22] M. Pallay, A.I. Ibrahim, R.N. Miles, S. Towfighian, Pairing electrostatic levitation with triboelectric transduction for high-performance self-powered MEMS sensors and actuators, Appl. Phys. Lett. 115 (13) (2019) 133503.
[23] F.M. Alsaleem, M.I. Younis, H.M. Ouakad, On the nonlinear resonances and dynamic pull-in of electrostatically actuated resonators, J. Micromech. Microeng. 19 (4) (2009) 045013.

[24] A.H. Nayfeh, B. Balachandran, Applied Nonlinear Dynamics: Analytical, Computational, and Experimental Methods, John Wiley & Sons, 2008.
[25] A. Cowen, B. Hardy, R. Mahadevan, S. Wilcenski, PolyMUMPs Design Handbook a MUMPs® process, MEMSCAP, 2011.
[26] M.I. Younis, F. Alsaleem, D. Jordy, The response of clamped–clamped microbeams under mechanical shock, Int. J. Non-Linear Mech. 42 (4) (2007) 643–657.
[27] K. Vummidi, M. Khater, E. Abdel-Rahman, A. Nayfeh, S. Raman, Dynamic pull-in of shunt capacitive MEMS switches, Proc. Chem. 1 (1) (2009) 622–625.
[28] F.M. Alsaleem, M.I. Younis, L. Ruzziconi, An experimental and theoretical investigation of dynamic pull-in in MEMS resonators actuated electrostatically, J. Microelectromech. Syst. 19 (4) (2010) 794–806.
[29] F. Najar, A. Nayfeh, E. Abdel-Rahman, S. Choura, S. El-Borgi, Nonlinear analysis of MEMS electrostatic microactuators: primary and secondary resonances of the first mode, J. Vib. Control 16 (9) (2010) 1321–1349.